Journal of Power Sources Advances 17-18 (2022) 100106

Contents lists available at ScienceDirect

Journal of Power Sources Advances

journal homepage: www.sciencedirect.com/journal/journal-of-power-sources-advances

X-ray absorption spectromicroscopy gives access to $Li_{1+x}Al_xGe_{2-x}(PO_4)_3$ (LAGP) local degradation at the anode-electrolyte interface

Majid Kazemian [a,*], Maya Kiskinova [b], Benedetto Bozzini [c]

[a] Diamond Light Source Ltd., Harwell Science and Innovation Campus, OX11 0DE, Didcot, Oxfordshire, UK
[b] Elettra – Sincrotrone Trieste S.C.p.A., S.S. 14-km 163.5 in Area Science Park, 34149, Basovizza, Trieste, Italy
[c] Department of Energy, Politecnico di Milano, via Lambruschini 4, 20156, Milano, Italy

ARTICLE INFO

Keywords:
LAGP
NASICON
All solid-state rechargeable batteries
STXM

ABSTRACT

Batteries with inorganic solid-state electrolytes (ISSE) are attracting notable interest for next-generation systems implementing Lithium (Li) metal anodes, in view of achieving higher energy densities combined with superior safety. Notwithstanding extensive research and development work, this technology is not yet ready for industrial implementation, one of the key challenges being the stability of ISSEs, chiefly at the anodic interface. This work attacks this issue for the specific case of the LAGP/Li (Lithium Aluminium Germanium Phosphate/Lithium) interface with a micro-spectroscopic approach centred on *post mortem* Scanning Transmission X-ray Microscopy (STXM) of intact LMO/LAGP/Li thin-film batteries, microfabricated in discharged state. Pristine and cycled cells were mapped to pinpoint morphochemical changes, induced by electrochemical ageing. The evidenced shape changes, corresponding to mechanical damaging of the solid/solid electrodic interfaces correlate with LAGP decomposition at the anode, leading to reduction of Ge, whereas the chemical state at the cathodic interface is preserved. Thanks to its submicron spacial resolution, the STXM at the Ge L-edge and O K-edge spectra allowed to assess the highly localized nature of the chemical transformation of LAGP and its correlation with the formation of Li outgrowth features.

1. Introduction

High energy density and safety are two crucial development lines for next-generation battery technologies and the combination of metallic Li anodes with inorganic solid-state electrolytes (ISSE) is a promising route to this goal. In fact, on the one hand, ISSEs are inflammable, and on the other hand, their combined single-ion conductivity and high stiffness are effective means to suppress Li dendrite growth. In addition to their general interest for battery technologies, ISSEs are enabling materials for thin-film SSBs (TFSSB), that can be microfabricated with approaches that are similar to those of microelectronic devices and, in particular, can prospectively provide micro-energy sources, integrated with micro-devices [1,2]. The downside of ISSEs is that they exhibit mechanical damaging and ionic contact issues at the solid electrode-electrolyte interfaces, dendrite growth control is poor in the presence of grain boundaries, and poorly understood decomposition processes impair ionic conductivity and can lead to undesirable mixed ionic-electronic conductivity. The development of pure ISSEs (i.e. without addition of polymers or ionic liquids) has a time-honoured history, that has been the object of several reviews (e.g. Refs. [3–6]). ISSEs can be classified into three main classes: (i) Phosphate-based - (i.a) (NASICON-type) LAGP $Li_{1+x}Al_xGe_{2-x}(PO_4)_3$ [7–9]; LATP $Li_{1.3}Al_{0.3}Ti_{1.7}(PO_4)_3$, [10–12]; (i.b) LiPON $Li_{2.88}PO_{3.73}N_{0.14}$ [13,14]; (ii) Oxide-based - (ii.a) Perovskite LLTO $Li_{3x}La_{2/3-x}\gamma_{1/3-2x}TiO_3$ (γ: vacancy) [15]; a typical stoichiometry being $Li_{0.34}La_{0.51}TiO_{2.94}$; (ii.b) anti-perovskite Li_3OX (X halogenide ion): $Li_3OCl_{0.5}Br_{0.5}$ [16]; $Li_{2.99}Ba_{0.005}OCl$ [17]; $Li_2(OH)_{0.9}F_{0.1}Cl$ [18]; (ii.c) Garnet LLZO $Li_7La_3Zr_5O_{12}$ [19]; $Li_7La_3Zr_5O_{12}/Li_{2.3}C_{0.7}B_{0.3}O_3$ [20]; $Li_{6.8}La_{2.95}Ca_{0.05}Zr_{1.75}Nb_{0.25}O_{12}$ [21]; (iii) Sulphide-based – (iii.a) Thio-LISICON-type LGPS $Li_{10}GeP_2S_{12}$ [22,23]; (iii.b) Binary sulfides $Li_2S{-}M_xS_y$ (M = Al, Si, P, etc.). $75Li_2S{\cdot}25P_2S_5$ [24]. In this work, we have focused on LAGP, a NASICON-type ISSE, for the reasons detailed in Section 2.1.

NASICON-type materials exhibit the general formula $AM_2(PO_4)_3$, in which A is a monovalent alkaline ion and M a tetravalent transition metal one. The structural framework can also be viewed as a rigid $M_2P_3O_{12}$ skeleton, where two MO_6 octahedra and three PO_4 tetrahedra are linked by sharing corner O atoms in single unit. Within this skeleton, alkali ions occupy the interstitial A1 and A2 sites and may diffuse via the

* Corresponding author.
E-mail address: Majid.kazemian@diamond.ac.uk (M. Kazemian).

https://doi.org/10.1016/j.powera.2022.100106
Received 26 August 2022; Received in revised form 18 October 2022; Accepted 26 October 2022
Available online 17 November 2022

transport channel established by MO_6 octahedra and PO_4 tetrahedra. Moreover, this structure can easily accommodate ion doping, enabling relatively flexible structural tuning. In addition, the special arrangement of metal-oxygen polyhedra minimizes electronic conductivity. A wide series of NASICON-type ISSEs have been proposed, mainly with $LiTi_2(PO_4)_3$ and $LiGe_2(PO_4)_3$ basic lattices, chiefly with partial substitution of tetravalent ions (i.e. Ti, Ge) with trivalent ones (Al, Ga, Fe), as well as other forms of doping [25]. Mainly, additives are used to modulate the crystal structure [26]; but also to generate glassy compounds that minimize diffusion barriers at grain boundaries [27]. Prototypical cases are LAGP $Li_{1+x}Al_xGe_{2-x}(PO_4)_3$, tackled in the present study, and LATP $Li_{1.3}Al_{0.3}Ti_{1.7}(PO_4)_3$. The relatively high Li^+ conductivity is attributed to the super-stoichiometry of this ion combined with the presence of tunnel structures exhibiting locally higher diffusion coefficients, associated with atomic radius effects.

As mentioned above, degradation – chemical, electrochemical, mechanical and thermal – is probably the single most critical issue impeding widespread practical implementation of ISSEs, the phosphate-type in particular. The most significant degradation modes of NASICON-type materials are summarized below. (i) Chemical stability of NASICON/cathode contact –decomposition, leading to Li_3PO_4 formation is found in the LAGP/LMN [28] and LATP/LCO, LMO, LPF [29] couples. (ii) Chemical stability of NASICON/Li contact – LATP/Li and LAGP/Li: formation of Li–Ti-Ge alloy at the interface, monitored by *ex situ* SEM and XPS [30,31]. (iii) Electrochemical stability of phosphate-based NASICON/Li contact – LAGP and LATP/Li interfaces were reported to undergo reduction of conductivity after a few hours of electrochemical polarization as a result of the reduction of Ti^{4+} and Ge^{4+} [32]. Reductive degradation leads to the formation of mixed electronically-ionically conducting (MEIC) layers [33]; sustaining continued reactivity. (iv) Mechanical stability - ISSEs are appealing as electrolytes for batteries with Li anodes, owing to their mechanical properties, since (single--crystal or with resistant GBs) electrolytes with shear modulus in excess of ca. a factor of 2 of that of Li (4.8 GPa) should prevent dendrite growth [34]. This requirement, in terms of intrinsic material properties, is met by all ISSEs, but, in practice, owing to a range of crystalline imperfections and MEIC nature, the practical impact on dendrite suppression is limited [35–37]. A mechanical aspect with ISSEs is that, in addition to electrical contact issues - that can also affect dendrite growth [38]; they must also be able to accommodate stresses resulting from battery fabrication and cycling [39]; whereby toughness properties come to the foreground [40]. (v) Thermal stability - even though ISSEs are considered the approach of choice to avoid thermal runaway, in the presence of Li metal cases of exothermal reactions and thermal runaway of LAGP have been reported [41]; attributed to oxygen, released from the chemically formed interface layer. Thermal stability of ISSEs is generally lowered when they are combined with cathode materials [29]. Degradation issues are at times faced by engineering the ISSE/anode interface, as: (i) compositional tuning (e.g. $LiZr_2(PO)_4$, to form a thin and stable interface layer containing Li_3P and Li_8ZrO_6, providing ion-transport channels and preventing the dendrite growth [42]; (ii) fabrication of interlayers (e.g. a LiF/Li_3N layer, via eletrochemical pre-cycling of LAGP/Li [43]; adding a sputtered Ge layer between LAGP and Li [44] and functionalized with Al_2O_3 layers the LATP surface in contact with Li [45] and Li_2O/Zn core-shell particles [46].

This complex degradation scenario of the ISSE and ISSE/electrode interfaces call for a more insightful physico-chemical understanding. Several approaches, documented in the literature and quoted in the previous paragraph, relate essentially to: (i) crystal structure (X-ray and neutron diffraction); (ii) particle morphology (SEM, TEM) and local atomic structure (HRTEM), combined with elemental (EDS) and electronic structure (EELS) information; (iii) Elemental and chemical-state composition (XAS, XPS, SIMS); (iv) Li^+-transport mechanisms (neutron scattering, NMR); (v) information regarding buried electrode/electrolyte interfaces by X-ray and neutron tomography as well as by micro-erosion techniques (ion sputtering, FIB). Moreover, *in situ* approaches are gaining momentum, such as: (i) XPS and/or AES, used e.g. to investigate the reduction of Ti and Ge by metallic Li and decomposition of LiPON [33,47,48]; to study the chemical stability of the $Li_7P_3S_{11}$/Li [49] and Li_6PS_5Cl/LCO, NMC and LMO [50] interfaces, to follow SEI formation in Li_2S–P_2S_5 [51]; (ii) neutron depth profiling (NDP), employed to analyse the garnet/Li interphase [52] and the dynamic evolution of Li^+ concentration profiles in LiPON, LLZO and amorphous Li_3PS_4 [37]; (iii) *in situ* electron holography to investigate the 2D electric potential distribution developing upon cycling [53] and Li^+ shuttling [54] in TFSSB, based on $Li_{1+x+y}Al_yTi_{2-y}Si_xP_{3-x}O_{12}$(LATSPO).

The present study demonstrates the feasibility and impact of soft-X ray based Near-Edge X-ray Absorption Fine Structure (NEXAFS) microspectroscopy to shed more light on the morpho-chemical evolution of ISSE electrolytes in complete batteries. The key challenge was building and operating a thin-film battery that allows sufficient soft-X ray transmission for accessing the NEXAFS L-edges of the metallic species, that are highly diagnostic in terms of electronic structure. In this first approach, where methodological aspects are the key, we worked with intact batteries in the *post mortem* mode in order to be able to assess the impact of prolonged cycling conditions not compatible with short synchrotron beamtimes, but exactly the same devices and approach can be adopted for follow-up *in operando* work.

2. Experimental

2.1. Battery microfabrication

This microspectroscopy study is focused on a microfabricated thin-film solid state battery (TFSSB), with LAGP ISSE. This kind of device, on the one hand belongs to a class of interest for battery-integrated microelectronics and, on the other hand, allows to cope with the soft-X ray transmission requirements of STXM microspectroscopy. The structure of a TFSSB includes: substrate, cathode collector, cathode, solid electrolyte, anode, anode collector, and protective coating.

The choice of LAGP as the ISSE was dictated by three key reasons: (i) its notable environmental stability, in fact NASICON-type materials are regarded as the most stable class of ISSEs with respect to environmental exposure and aqueous processing [55–57]; (ii) LAGP exhibits a wide electrochemical window (3.0–4.6V was demonstrated in a LMO/LAGP/Li TFSSB [58]) and (iii) Ge and Al possess absorption edges in the soft-X ray range. Finally, thin-film NASICON-type ISSEs have been successfully deposited by Magneton-Sputtering PVD [59] and PLD in Ref. [14]. As far as the anode is concerned, we selected the so-called anodeless fabrication concept, whereby Li is plated *in situ* during the first charge cycle. This fabrication approach combines the high-energy density capability of a metallic Li anode with ease of assembly, thanks to the absence of reactive materials [60,61]; of course at the cost of an early tendency to grow granular, mossy or dendritic Li. In the specific case of this study, this fabrication was dictated by two main reasons: (i) safe transfer to synchrotron endstations, that are not equipped with proper ambient allowing sample insertion under controlled atmosphere; (ii) difficulty to grow a Li film by vapour deposition and apply wire contact, owing to the low melting point of Li. The anodic current collector and support for Li plating was Cu, as customary in anodeless Li batteries, since this element allows blocking of Li diffusion. $LiMn_2O_4$ (LMO) was selected among the most widely employed TFSBB cathodes because of its ambient stability and ease of microfabrication, though at the cost of a complex intercalation chemistry, with two main phase transformations during each deep charge-discharge cycle. Thin-film LMO cathodes have been successfully grown by PVD (MS [62] and PLD [63]), as well as Plasma-enhanced CVD [64]. Moreover, it is worth noting that the thin-film cathode up to thicknesses of a few μm, well above that employed in our device [65]; affects negligibly the cell resistance.

Specifically, thin films of the patterned electrodes (Cathode; Mn-

based spinel $LiMn_2O_4$ LMO) and electrolyte (NASICON-type; $Li_{1.5}Al_{0.5}Ge_{1.5}(PO_4)_3$ (LAGP)) were directly grown and nanofabricated by a four-step optical lithography process and lift-off on commercial suspended Si_3N_4 membranes (dimensions: square support, side 5.0 mm; square window, side 500 μm; window thickness 75 nm - supplied by Silson Ltd. UK) with thickness optimised for X-ray transmission at I08 beamline, bearing evaporated Au or Cu (for the anode-free technology) current feeders. We implemented a planar configuration with partial electrode-electrolyte overlap to maximize the sensitivity to electrode-electrolyte interfacial processes and space-dependent intercalation/plating into/onto the electrodes (Fig. 1).

Moreover, the highly ambient-stable LAGP layer, covering whole device, also acted as a soft-X ray transparent protective coating. The Electrical contacts are first realized by sputtering Cr (10 nm)/Au (30 nm) layers (Z400 sputtering system, Leybold GmbH). Au current collectors have been successfully used in TFSSBs [66]. Afterwards, both LMO and Cu electrodes are deposited on top by electron beam evaporation (BAK 640 evaporator, Evatec AG) to a final thickness of 50 nm with a deposition rate of 0.2 nm/s and 2 nm/s, respectively, yielding nanocrystalline cathode material that is expected to cycle well in the range 4.5 ÷ 3.0 V (see Section 2.2) at room temperature [13]. Better cathode performance would be enabled by annealing [67]; but this would destroy the optical window. Moreover, interaction of LMO with the ISSEs can be expected [68]. Finally, 100 nm LAGP electrolyte is deposited from a stoichiometric target by RF sputtering (Z400 sputtering system, Leybold GmbH) in a pure Ar atmosphere (4×10^{-2} mbar) [7]. LAGP deposition was carried out in planar geometry with a substrate/target distance of 40 mm and a power density of 1.7 W/cm^2, yielding a deposition rate of 5.0 nm/min. To preserve the P/Ge ratio in LAGP thin films we have followed the protocol reported in the literature [69]. The individual nanofabricated devices were wire bonded on an IC socket adapter (Fig. 1-C).

The SEM images of the topmost LAGP layer (Fig. 2(A&B) show a homogeneous layer with a micro-crystallite pattern. EDX maps and quantitative analyses performed after the LMO and the LAGP deposition steps (Fig. 2(C&F)) confirm the stoichiometry of the target compounds.

The structure of the functional layer of the as-fabricated batteries was checked by XRD (Fig. 2(D)) and Raman spectroscopy (Fig. 2(E)) Though yielding complex diffractograms, with a strong Si background and overlap of the reflections from all phases present in the thin-film battery, XRD is shedding light on the structure of the micro-fabricated electrode and electrolyte assembly of SSBs as reported in Ref. [70]. Reflections from the Cu (PDF 003–1018) and LMO (PDF 35–0782) electrodes and from the LAGP electrolyte are seen, together with peaks from the partly polycrystalline Si substrate [71]; the Si_3N_4 window [72] and Al (PDF 85–1327) from sample-holder clips, that exhibit peak shifts owing to the zero-error caused by being out of the sample plane. LMO [73] and LAGP [9,74–77], appear well-crystallized. The Raman spectrum has a relatively low signal-to-noise ratio owing to a strong fluorescence background (removed in the spectrum shown), but the quality of the spectrum is very similar to those reports in the literature [76,77]. The Raman spectrum of LAGP exhibits features that are characteristic of NASICON-type materials, and are dominated by the vibrational modes of PO_4 units [78–80]; in particular: (A) translation-libration of PO_4 tetrahedra phosphate tetrahedral; P–O–P symmetrical (B) and anti-symmerical (C) bending and (D) stretching of PO_4 tetrahedra.

2.2. Scanning soft-X ray transmission (STXM) microspectroscopy

The STXM measurements were carried out at I08-SXM beamline in Diamond Light Source Ltd. located in Didcot, UK which is hosting a Scanning Transmission X-ray Microscope (STXM) [81]. The sample is raster-scanned in a plane perpendicular to the focused X-ray beam formed by a Fresnel zoneplate (ZP) and the transmitted X-rays are detected using an avalanche photodiode for obtaining images. With the available optics configuration we used beam size of 100 nm and 200 nm have been formed at Ge L-edge and O K-edge, respectively, which defining the spatial resolution achieved for this experiment. From the stack of images acquired over the energy windows across Ge, O and other absorption edges, μ-XAS spectra were extracted using

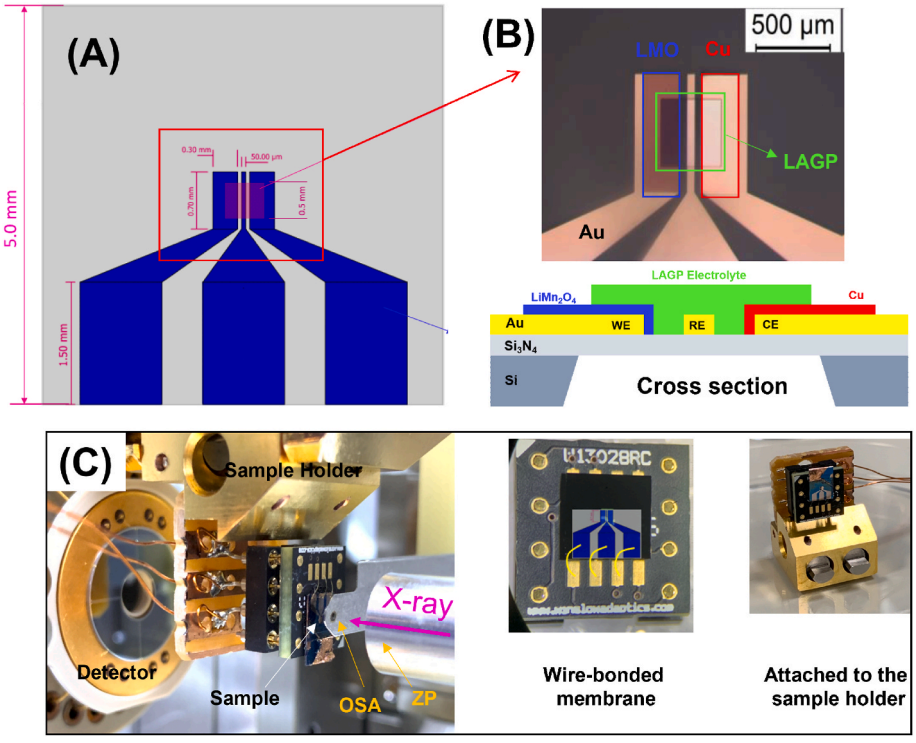

Fig. 1. – Design (A–B) of the thin-film solid-state batteries for STXM. (C) Assembly of nanofabricated battery and its mounting on the sample stage. OSA (order sorting aperture) and ZP (zone plate).

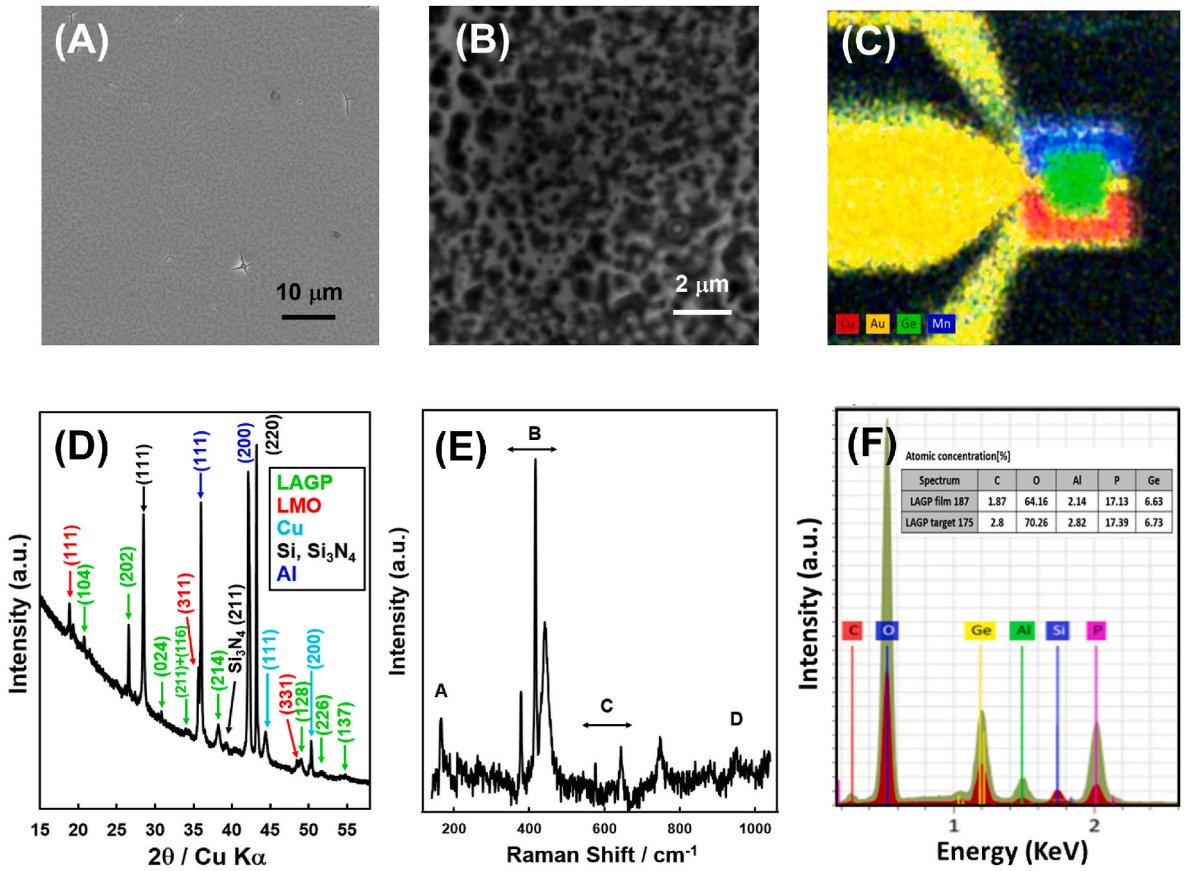

Fig. 2. – (A&B) SEM images of LAGP deposited layer; (C&F) EDX maps and spectra. (D) XRD and (E) Raman spectrum of nanofabricated battery (Excitation laser: 785 nm).

post-processing software. We used a dwell time of 10 msec per pixel to acquire the STXM images. This takes around 30–60 Sec to image a 50 × 50 pixel square of a region of interest (ROI) and around 60min for stack of images over the edge energies including overhead time. The intensity of incident beam (I0) was measured by moving sample out of the beam with the same optics set-up used for absorption signal (I) measurements. The central theme of the I08-SXM beamline is the ability to obtain morphological, chemical speciation and chemical state information on a full range of materials (inorganic/organic) under real conditions.

The I08 sample holder is modified to accommodate an IC Dip Socket with 3 wire connections for biasing the battery cell using an electrical feed-through on the end-station chamber. Stacks of STXM images were collected with 0.1 eV energy steps for pristine and cycled samples, by scanning the energy across the Ge L-edges and O K-edge in the ranges: 630–670 eV, 1215–1235 eV and 520–570 eV, respectively.

2.3. Data analysis and μ-XAS data post-processing

The performed analysis of the μ-XAS data is to (i) reveal the Ge and O chemical-state and study the formation of oxidation intermediates and (ii) assigning the mass transport at electrode|electrolyte interface. MANTiS software program is employed for data post-processing to elaborate the STXM results acquired in the form of stack images [82]. It is a versatile software package specifically developed for STXM data analysis to extract chemical-state distribution maps and normalized NEXAFS spectra corresponding to the diagnostic energies over region of interests.

3. Results and discussion

The battery, fabricated in a discharged state with a bare Cu current feeder at the anodic terminal, was initially charged by de-intercalating Li from the spinel cathode and plating Li on the Cu film and then cycled as detailed in Section 3.1. A pristine replicate of the battery and of the cycled one were studied by STXM presented in Section 3.2, following the morpho-chemical changes undergone by LAGP as a result of electrochemical ageing.

3.1. Electrochemical ageing

Before the initial charge, the pristine battery is stable in air and can be safely moved from the lab to the glove-box for ageing. Transfer from the glove-box to the optical and soft-X ray microscopes implies limited air exposure periods, whereby, in principle, the protective layer should minimize the oxidation of residual plated Li. The cell was electrochemically cycled between 4.5 and 3.0 V in an Ar-filled glove-box, using an SP 50e Bio-logic potentiostat. The electrochemical preparation of the *ex-situ* aged cell involved 5 charge-discharge cycles, terminating in the discharged state. In order to drive the microcell under electrochemical conditions without activating parasitic reactions, charge and discharge were performed by applying 4.5 and 3.0 V for periods of 24 h. This ensured current relaxation to vanishing values: charging at potentials not exceeding 4.5 V avoids major changes in lattice structure [13] and the feasibility of prolonged LMO/LiPON/Li TFSSBs cycling in this range was reported [83]. In principle, complete stripping of electroplated Li is reversible, and since no Li excess is present, the Li-free battery should not be damaged by over-discharging the LMO cathode, in contrast to conventional Li-LMO batteries. The potentiostatic control adds further safety from this viewpoint, even though irreversible phase transitions upon lithiation-delithiation of the spinel structure still might occur. The capacity and cathode utilization were simply estimated from the integral of the relaxing part of the chronoamperometric time-series, yielding the

values plotted in Fig. 3-A.

As shown in Fig. 3-A, the Li-free TFSSB lost over 50% of its initial specific charge capacity at 4.5 V after the first discharge at 3.0 V. This loss is ca. a factor of 6 higher than those of thin-film devices designed for optimal battery performance [62]; in which thicker materials were employed but in the present case we have to secure the soft-X ray transmission. We monitored the progressive shape changes of both the anode/electrolyte and cathode/electrolyte interfaces after each cycle by OM: the results are reported in Fig. 3-B&C.

The OM micrographs of Fig. 3 show the surface of: (B) the cathode/electrolyte (LMO/LAGP) and (C) anode/electrolyte (Li@Cu/LAGP) interfaces of the TFSSB cell in the pristine state and after each of the five charge-discharge cycles. One can quite clearly notice the progressive formation of interfacial morphology between the electrolyte and both the cathode and (panel (B) and the anode (panel (C)). In the former case, a decohesion layer, accompanied by the grow of cavities from the LAGP into the LMO, while in the latter new globular objects appear on both sides of the interface. The morphology change of the cathode in vicinity of LAGP is caused by mechanical damaging due the volume changes during LMO lithiation/delithiation cycles, exacerbated by the solid/solid contact with LAGP. Instead the formation of globular crystallites, without appreciable formation of pores or voids at the Li@Cu/LAGP interface, is related to Li plating/stripping and is in accordance with the results of a systematic study on mesoscopic Li film electrode morphology evolution, based on OM, SEM and profilometry in TFSSBs [83]: the specific anode morphology resembles the "agglomerate" type, characteristic of uncoated TFSSB and is compatible with the possibly limited protection by the LAGP capping layer.

3.2. Elemental and chemical mapping by X-ray absorption microscopy

The battery, both in the pristine and cycled states was studied by STXM. In the pristine state, the cathode and the electrolyte were found to be homogeneous confirming the as-fabricated Ge oxidation state. After cycling, only morphological changes, as those observed by OM (Fig. 3-B), were evidenced at the cathodic LMO/LAGP interface, while at the anodic (Li@Cu/LAGP) interface important morphological, compositional and chemical-state variations were noticed. As shown in Fig. 4, they are comprising: (i) the build-up of material, coherently with the OM images and the expected irreversible Li plating/stripping process; (ii) evolution of the Ge L-edge spectra denoting Ge reduction [84–88] and (iii) variations in the O K-edge spectra (a new peak at 534 eV), in correspondence with the accumulated material layer. The measured spectral modifications and in keeping with literature spectra corresponding to Li_2O [89] and GeO_2 (modification of main peak at ca. 540 eV and change in slope on the low-energy side of the spectrum) [88]. Formation of these species is coherent with the received scenario regarding LAGP degradation. Early reports implementing LiPON-type SSE [60]; based on SEM imaging, upon cycling the formation of a new phase at the anode of a Cu/LiPON/LCO cell TF-SSBs, was explained, without going into mechanistic details, with the growth of Li_2O crystallites, as a result of electrolyte decomposition accompanying Li plating. This process was correlated with the loss of active lithium inventory. This in turn, correlates with capacity fade, accompanied by anode passivation. More recently, the degradation of LAGP in contact with Li, simulating *ex situ* the electrolyte/anode chemistry, was explicitly addressed on the basis of space-averaged XPS analyses.

Ge chemical-state changes with respect to pristine conditions clearly indicate reductive degradation characterized by the formation of metallic Ge and Ge–Li alloys. The LAGP/Li contact was obtained by evaporating Li on a LAGP sample [30] or contacting LAGP with liquid Li [31]. Similarly, for the case of LATGP, Hartmann et al. [30] pinpointed the same kind of damaging, due to reduction of both Ge and Ti and alloy formation with Li. It is worth noting that, on the basis of purely electrochemical data, Liu et al. [44] reported that sputter-coating LAGP with a thin layer of Ge would lead to the formation of a Li–Ge buffer layer suppressing further Ge^{4+} reduction. Cognate XPS results were obtained with the LLTO perovskite with Li sputtered on top, as a result of which Ti^{3+} and Ti^0 were reported to form from Ti^{4+} [33]. At variance with Ge and Ti in phosphate-based LAGP and LATGP and perovskite LLTO, the chemical state of Zr in garnet LLZO seems to be more stable: contact with molten Li was reported not to result in reduction [90]; while Li sputtering onto Nb- and Ta-doped LLZO was reported to lead to formation of Nb^{3+} and Nb^{4+} from Nb^{5+} and Zr^{2+} from Zr^{4+}, while the chemical state of Ta was stable [91]. Moreover, on the basis of Ge K-edge spectroscopy, Cao et al. [92] reported the reduction of Ge resulting from Li insertion into Li $NbGeO_5$ LIB anodes.

If these studies yield indirect information on the initial state of LAGP-based batteries fabricated with metallic anodes or anodeless batteries subject to the first charge cycle, no clue is obtained regarding the fate of reduced Ge upon electrochemical cycling. In fact, on the one hand, Ge reduction during charging leads to decomposition of the mixed phosphate, on the other hand discharge might give rise to the oxidation of elemental Ge in the metallic or alloyed forms. Depending on the details of the chemical evolution of decomposed phosphate, Li- and Ge-oxides could form, coherently with our observations of Fig. 4, that report for the first-time results concerning the electrochemically cycled LAGP/Li interface. A first step into a better understanding of this complex material evolution is for sure the spectral imaging approach proposed in this work. In fact, Neudecker et al. [60] reported interface evolution

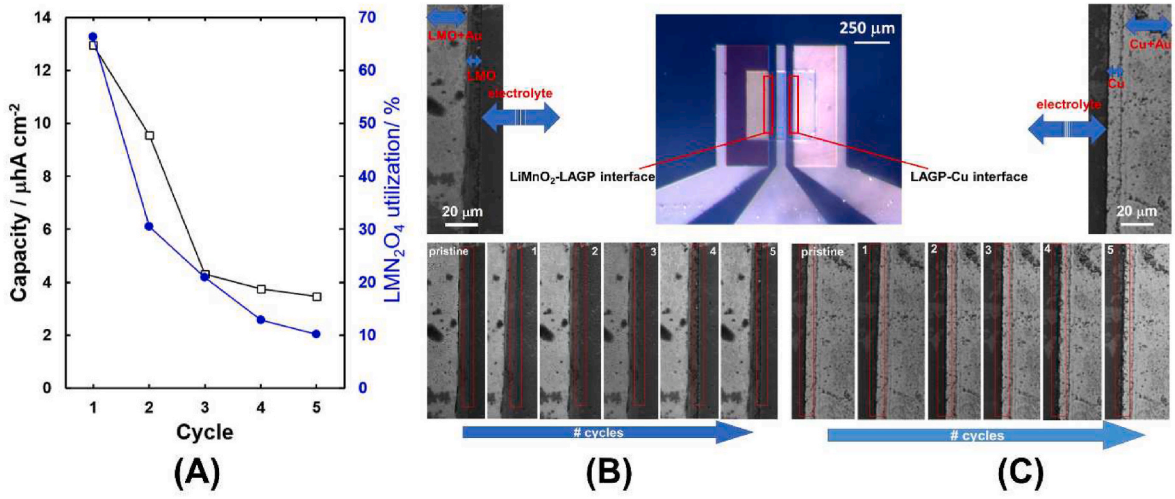

Fig. 3. – (A) Capacity and cathode utilization for the cell-ageing experiment. (B) Left: cathode/electrolyte interface, (C) Right: anode/electrolyte interface.

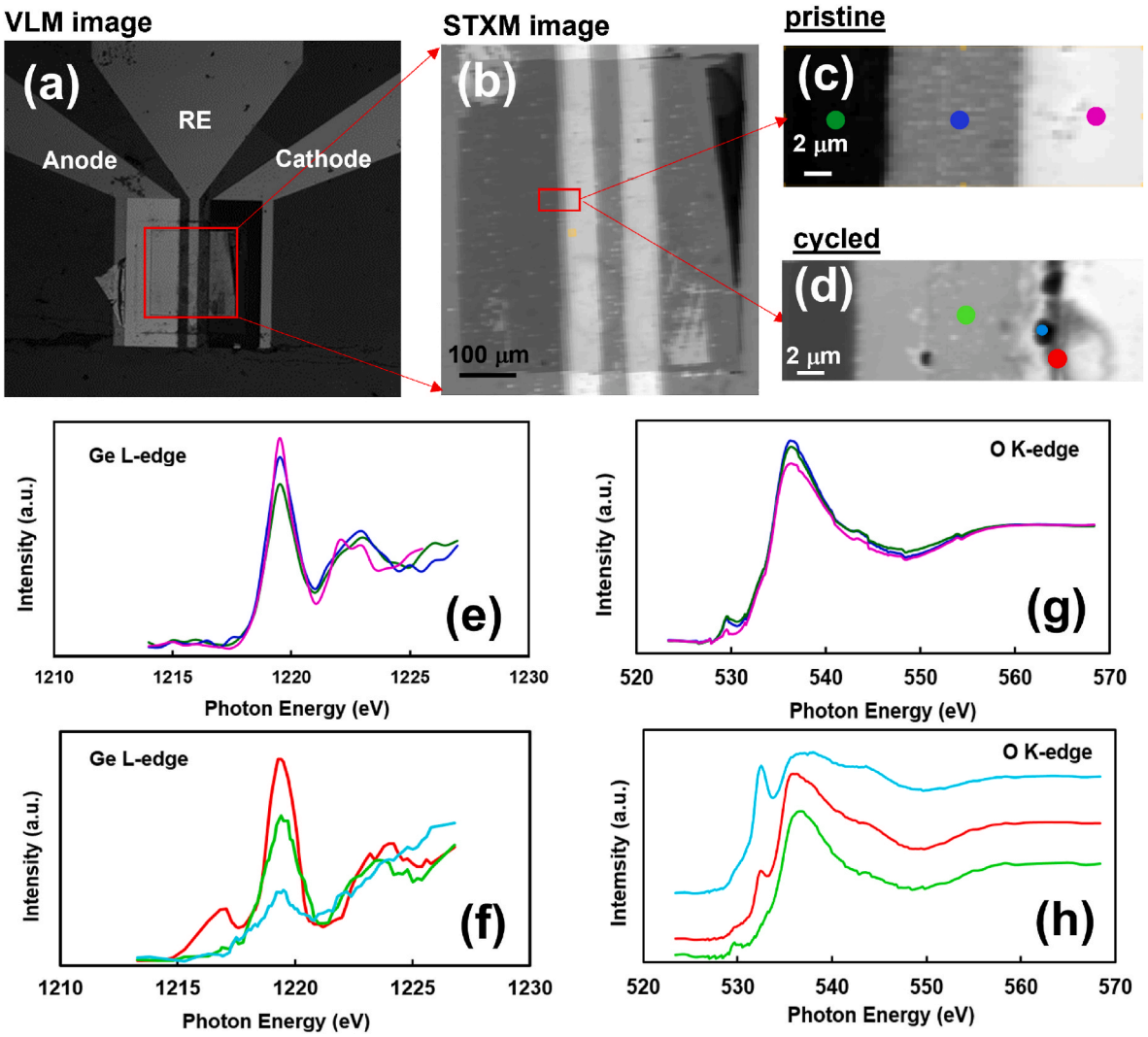

Fig. 4. (a) Visible light microscope (VLM) image from the cell and STXM image over membrane window showing electrodes configuration. (b,c and d) magnified STXM images of Anode-electrolyte interface from sample in pristine status and after cycling. Ge L-edge (e,f) and O K-edge (g,h) spectra from sample in pristine condition and after cycling. The spectra were extracted from stacks of images.

based on SEM imaging, but without chemical information, while the XPS and EXAFS literature studies at the Ge 3d and Ge K-edge, cited above, yield chemical-state details, but without information on their localization. Here, we pinpoint the close correspondence between the morphological variations and the regions where Ge and O absorption spectra undergo changes: Ge reduction and the formation of the new oxide state (Fig. 4-B, light-blue spot) appear exactly in correspondence of the morphologically transformed zone at the anode/electrolyte interface.

4. Conclusions

The present scanning Transmission soft-X ray microscopy (STXM) results outline the morphochemical changes of LAGP occurring in a thin-film solid-state battery as a result of cycling. They provide a consistent scenario of Ge reduction, with possible Ge–Li alloy formation, which accompany the evident morphological variations occurring at the electrode-electrolyte interface. Interestingly, even though notable structural changes were evidenced at both the solid/solid cathodic and anodic interfaces the Ge chemical state changes occur only at the anode, where Li is plated during battery charging. In the context of a real battery, our submicrometer space resolution results confirm that the reductive damaging mechanism, proposed in the literature on the basis of homogeneous chemical lithiation of LAGP, is actually operative at the Li/LAGP interface as well. Moreover, the battery fabrication experience developed and the understanding of instrumental response gained in this study provides concrete handles to move on to dynamic *in operando* experiments, during soft-X ray absorption measurements.

Declaration of competing interest

The authors declare that they have no known competing financial interests or personal relationships that could have appeared to influence the work reported in this paper.

Data availability

Data will be made available on request.

Acknowledgements

The STXM measurements at I08 beamline and sample materials were performed at Diamond Light Source Ltd. [beam time MG26226-1].

Device fabrication was performed at Polifab, the micro and nano-fabrication facility of Politecnico di Milano.

References

[1] Sébastien Moitzheim, Brecht Put, M. Philippe, Vereecken, Advances in 3D thin-film Li-ion batteries, Adv. Mater. Interfac. **6** (2019), 1900805.

[2] Min Koo, Kwi-Il Park, Seung Hyun Lee, Minwon Suh, Duk Young Jeon, Jang Wook Choi, Kisuk Kang, Keon Jae Lee, Bendable inorganic thin-film battery for fully flexible electronic systems, Nano Lett. 12 (9) (2012) 4810–4816.

[3] C. Li, et al., An Advance Review of Solid-State Battery: Challenges, Progress and Prospects" Sustainable Materials and Technologies, vol. 29, 2021, e00297.

[4] R. Chen, et al., Approaching Practically Accessible Solid-State Batteries: Stability Issues Related to Solid Electrolytes and Interfaces" Chem vol. **120**, Rev., 2020, pp. 6820–6877.

[5] Q. Zhao, et al., Designing solid-state electrolytes for safe, energy-dense batteries" Nature Reviews/Materials 5 (2020) 229–252.

[6] F. Zheng, et al., Review on Solid Electrolytes for All-Solid-State Lithium-Ion Batteries" Journal of Power Sources, vol. 389, 2018, pp. 198–213.

[7] Zhijian Sun, et al., Preparation and ion conduction of Li_1.5Al0.5Ge1.5(PO4)3 solid electrolyte films using radio frequency sputtering, Solid State Ionics 346 (2020), 115224.

[8] Rachel DeWees, Prof Hui Wang, Synthesis and Properties of NaSICON-type LATP and LAGP Solid Electrolytes ChemSusChem, vol. 12, 2019, pp. 3713–3725.

[9] Y. Meesala, et al., All-solid-state Li-ion battery using Li1.5Al0.5Ge1.5(PO4)3 as electrolyte without polymer interfacial adhesion, J. Phys. Chem. C 122 (2018) 14383–14389.

[10] Y.-C. Kim, et al., Improving the ionic conductivity of Li1+xAlxGe2-x(PO4)3 solid electrolyte for all-solid-state batteries using microstructural modifiers Ceramics, International 46 (14) (2020) 23200–23207.

[11] K. Waetzig, et al., Synthesis and sintering of Li1.3Al0.3Ti1.7(PO4)3 (LATP) electrolyte for ceramics with improved Li+ conductivity, J. Alloys Compd. (2020) 818 153237.

[12] G. Yan, et al., Influence of sintering temperature on conductivity and mechanical behavior of the solid electrolyte LATP, Ceram. Int. 45 (12) (2019) 14697–14703.

[13] J.B. Bates, N.J. Dudney, B. Neudecker, A. Ueda, C.D. Evans, Thin-film Lithium and Lithium-Ion Batteries" Solid State Ionics, vol. 135, 2000, pp. 33–45.

[14] Y. Hamon, A. Douard, F. Sabary, C. Marcel, P. Vinatier, B. Pecquenard, A. Levasseur, Influence of sputtering conditions on ionic conductivity of LiPON thin films, Solid State Ionics 177 (2006) 257–261.

[15] C. Uhlmann, et al., Interface and grain boundary resistance of a lithium lanthanum titanate (Li3xLa2/3−xTiO3, LLTO) solid electrolyte, J. Power Sources 307 (2016) 578–586.

[16] Y. Zhao, L.L. Daemen, Superionic conductivity in lithium-rich anti-perovskites, J. Am. Chem. Soc. **134** (2012) 15042–15047.

[17] M.H. Braga, J.A. Ferreira, V. Stockhausen, J.E. Oliveira, A. El-Azab, Novel Li_3ClO based glasses with superionic properties for lithium batteries, J. Mater. Chem. **2** (2014) 5470–5480.

[18] Y. Li, W. Zhou, S. Xin, S. Li, J. Zhu, X. Lü, Z. Cui, Q. Jia, J. Zhou, Y. Zhao, et al., Fluorine-doped antiperovskite electrolyte for all-solid-state lithium-ion batteries, Angew. Chem., Int. Ed. **55** (2016) 9965–9968.

[19] (27) R. Murugan, V. Thangadurai, W. Weppner, Fast lithium ion conduction in garnet-type $Li_7La_3Zr_2O_{12}$, Angew. Chem., Int. Ed. 46 (2007) 7778–7781.

[20] F. Han, J. Yue, C. Chen, N. Zhao, X. Fan, Z. Ma, T. Gao, F. Wang, X. Guo, C. Wang, Interphase engineering enabled all-ceramic lithium battery, Joule **2** (2018) 497–508.

[21] (56) S. Ohta, J. Seki, Y. Yagi, Y. Kihira, T. Tani, T. Asaoka, Co-sinterable lithium garnet-type oxide electrolyte with cathode for all-solid-state lithium ion battery, J. Power Sources 265 (2014) 40–44.

[22] Y. Kato, S. Hori, T. Saito, K. Suzuki, M. Hirayama, A. Mitsui, M. Yonemura, H. Iba, R. Kanno, High-power all-solid-state batteries using sulfide superionic conductors, Nat. Energy **1** (2016), 16030.

[23] W.B. Zhang, D.A. Weber, H. Weigand, T. Arlt, I. Manke, D. Schroder, R. Koerver, T. Leichtweiss, P. Hartmann, W.G. Zeier, et al., Interfacial processes and influence of composite cathode microstructure controlling the performance of all-solid-state lithium batteries, ACS Appl. Mater. Interfaces **9** (2017) 17835–17845.

[24] T. Ohtomo, A. Hayashi, M. Tatsumisago, Y. Tsuchida, S. Hama, K. Kawamoto, All-solid-state lithium secondary batteries using the $75Li_2S \bullet 25P_2S_5$ glass and the $70Li_2S \bullet$ 30P2S5 glass-ceramic as solid electrolytes, J. Power Sources 233 (2013) 231–235.

[25] M. Giarola, A. Sanson, F. Tietz, S. Pristat, E. Dashjav, D. Rettenwander, G. J. Redhammer, G. Mariotto, Structure and vibrational dynamics of nasicon-type $LiTi_2(PO_4)_3$, J. Phys. Chem. C **121** (2017) 3697–3706.

[26] L. Xiong, Z. Ren, Y. Xu, S. Mao, P. Lei, M. Sun, LiF assisted synthesis of $LiTi_2(PO_4)_3$ solid electrolyte with enhanced ionic conductivity, Solid State Ionics 309 (2017) 22–26.

[27] J. Fu, Fast Li+ ion conducting glass-ceramics in the system $Li_2O-Al_2O_3-GeO_2-P_2O_5$, Solid State Ionics **104** (1997) 191–194.

[28] J.P. Robinson, P.D. Kichambare, J.L. Deiner, R. Miller, M.A. Rottmayer, G. M. Koenig, High temperature electrode-electrolyte interface formation between $LiMn_{1.5}Ni_{0.5}O_4$ and $Li_{1.4}Al_{0.4}Ge_{1.6}(PO_4)_3$, J. Am. Ceram. Soc. **101** (2018) 1087–1094.

[29] M. Gellert, E. Dashjav, D. Gruner, Q.L. Ma, F. Tietz, Compatibility study of oxide and olivine cathode materials with lithium aluminum titanium phosphate, Ionics **24** (2018) 1001–1006.

[30] P. Hartmann, T. Leichtweiss, M.R. Busche, M. Schneider, M. Reich, J. Sann, P. Adelhelm, J. Janek, Degradation of NASICON-type materials in contact with lithium metal: formation of mixed conducting interphases (MCI) on solid electrolytes, J. Phys. Chem. C **117** (2013) 21064–21074.

[31] L. He, et al., Failure mechanism and interface engineering for NASICON structured all-solid-state lithium metal batteries, ACS Appl. Mater. Interfaces 11 (2019) 20895–20904.

[32] J.K. Feng, L. Lu, M.O. Lai, Lithium storage capability of lithium ion conductor $Li_{1.5}Al_{0.5}Ge_{1.5}(PO_4)_3$, J. Alloys Compd. 501 (2010) 255–258.

[33] S. Wenzel, T. Leichtweiss, D. Kruger, J. Sann, J. Janek, Interphase formation on lithium solid electrolytes-an in situ approach to study interfacial reactions by photoelectron spectroscopy, Solid State Ionics 278 (2015) 98–105.

[34] C. Monroe, J. Newman, The impact of elastic deformation on deposition kinetics at lithium/polymer interfaces, J. Electrochem. Soc. **152** (2005) A396–A404.

[35] L. Porz, T. Swamy, B.W. Sheldon, D. Rettenwander, T. Froemling, H.L. Thaman, S. Berendts, R. Uecker, W.C. Carter, Y.-M. Chiang, Mechanism of lithium metal penetration through inorganic solid electrolytes, Adv. Energy Mater. **7** (2017), 1701003.

[36] T. Swamy, R. Park, B.W. Sheldon, D. Rettenwander, L. Porz, S. Berendts, R. Uecker, W.C. Carter, Y.-M. Chiang, Lithium metal penetration induced by electrodeposition through solid electrolytes: example in single-crystal $Li_6La_3ZrTaO_{12}$ garnet, J. Electrochem. Soc. **165** (2018) A3648–A3655.

[37] F. Han, A.S. Westover, J. Yue, X. Fan, F. Wang, M. Chi, D.N. Leonard, N.J. Dudney, H. Wang, C. Wang, High electronic conductivity as the origin of lithium dendrite formation within solid electrolytes, Nat. Energy **4** (2019) 187–196.

[38] T. Krauskopf, R. Dippel, H. Hartmann, K. Peppler, B. Mogwitz, F.H. Richter, W. G. Zeier, J. Janek, Lithium-metal growth kinetics on LLZO garnet-type solid electrolytes, Joule **3** (2019) 2030–2049.

[39] A. Mukhopadhyay, B.W. Sheldon, Deformation and stress in electrode materials for Li-ion batteries, Prog. Mater. Sci. 63 (2014) 58–116.

[40] F.P. McGrogan, T. Swamy, S.R. Bishop, E. Eggleton, L. Porz, X. Chen, Y.-M. Chiang, K.J. Van Vliet, Compliant yet brittle mechanical behavior of $Li_2S-P_2S_5$ lithium-ion-conducting solid electrolyte, Adv. Energy Mater. **7** (2017), 1602011.

[41] H. Chung, B. Kang, Mechanical and thermal failure induced by contact between a $Li_{1.5}Al_{0.5}Ge_{1.5}(PO_4)_3$ solid electrolyte and Li metal in an all solid-state Li cell, Chem. Mater. 29 (2017) 8611–8619.

[42] Y. Li, W. Zhou, X. Chen, X. Lü, Z. Cui, S. Xin, L. Xue, Q. Jia, J.B. Goodenough, Mastering the interface for advanced all-solid-state lithium rechargeable batteries, Proc. Natl. Acad. Sci. U.S.A. 113 (2016) 13313–13317.

[43] G.M. Hou, X.X. Ma, Q.D. Sun, Q. Ai, X.Y. Xu, L.N. Chen, D.P. Li, J.H. Chen, H. Zhong, Y. Li, et al., Lithium dendrite suppression and enhanced interfacial compatibility enabled by an ex situ SEI on Li anode for LAGP-based all-solid-state batteries, ACS Appl. Mater. Interfaces **10** (2018), 18610.

[44] Y.J. Liu, C. Li, B.J. Li, H.C. Song, Z. Cheng, M.R. Chen, P. He, H.S. Zhou, Germanium thin film protected lithium aluminum Germanium phosphate for solid-state Li batteries, Adv. Energy Mater. 8 (7) (2018), 1702374.

[45] Y.L. Liu, Q. Sun, Y. Zhao, B.Q. Wang, P. Kaghazchi, K.R. Adair, R.Y. Li, C. Zhang, J. R. Liu, L.Y. Kuo, et al., Stabilizing the interface of NASICON solid electrolyte against Li metal with atomic layer deposition, ACS Appl. Mater. Interfaces 10 (37) (2018), 31240.

[46] X.G. Hao, Q. Zhao, S.M. Su, S.Q. Zhang, J.B. Ma, L. Shen, Q.P. Yu, L. Zhao, Y. Liu, F. Y. Kang, Y.B. He, Constructing multifunctional interphase between $Li_{1.4}Al_{0.4}Ti_{1.6}(PO_4)_3$ and Li metal by magnetron sputtering for highly stable solid-state lithium metal batteries, Adv. Energy Mater. **9** (2019), 1901604.

[47] S. Wenzel, S. Randau, T. Leichtweiss, D.A. Weber, J. Sann, W.G. Zeier, J. Janek, Direct observation of the interfacial instability of the fast ionic conductor $Li_{10}GeP_2S_{12}$ at the lithium metal anode, Chem. Mater. **28** (2016) 2400–2407.

[48] A. Schwobel, R. Hausbrand, W. Jaegermann, Interface reactions between LiPON and lithium studied by in-situ X-ray photoemission, Solid State Ionics 273 (2015) 51–54.

[49] S. Wenzel, D.A. Weber, T. Leichtweiss, M.R. Busche, J. Sann, J. Janek, Interphase formation and degradation of charge transfer kinetics between a lithium metal anode and highly crystalline $Li_7P_3S_{11}$ solid electrolyte, Solid State Ionics 286 (2016) 24–33.

[50] J. Auvergniot, et al., Interface stability of argyrodite Li_6PS_5Cl toward $LiCoO_2$, $LiNi_{1/3}Co_{1/3}Mn_{1/3}O_2$, and $LiMn_2O_4$ in bulk all-solid-state batteries, Chem. Mater. **29** (2017) 3883–3890.

[51] K.N. Wood, K.X. Steirer, S.E. Hafner, C.M. Ban, S. Santhanagopalan, S.H. Lee, G. Teeter, Operando X-ray photoelectron spectroscopy of solid electrolyte interphase formation and evolution in $Li_2S-P_2S_5$ solid-state electrolytes, Nat. Commun. 9 (2018) 2490.

[52] C. Wang, Y. Gong, J. Dai, L. Zhang, H. Xie, G. Pastel, B. Liu, E. Wachsman, H. Wang, L. Hu, In situ neutron depth profiling of lithium metal-garnet interfaces for solid state batteries, J. Am. Chem. Soc. 139 (2017) 14257–14264.

[53] K. Yamamoto, Y. Iriyama, T. Asaka, T. Hirayama, H. Fujita, C.A.J. Fisher, K. Nonaka, Y. Sugita, Z. Ogumi, Dynamic visualization of the electric potential in an all-solid-state rechargeable lithium battery, Angew. Chem., Int. Ed. 49 (2010) 4414–4417.

[54] K. Yamamoto, Y. Iriyama, T. Asaka, T. Hirayama, H. Fujita, K. Nonaka, K. Miyahara, Y. Sugita, Z. Ogumi, Direct observation of lithium-ion movement around an in-situ-formed-negative-electrode/solid-state-electrolyte interface during initial Charge−Discharge reaction, Electrochem. Commun. **20** (2012) 113–116.

[55] T. Zhang, N. Imanishi, Y. Shimonishi, A. Hirano, Y. Takeda, O. Yamamoto, N. Sammes, A novel high energy density rechargeable lithium/air battery, Chem. Commun. **46** (2010) 1661–1663.

[56] Y. Shimonishi, T. Zhang, N. Imanishi, D. Im, D.J. Lee, A. Hirano, Y. Takeda, O. Yamamoto, N. Sammes, A study on lithium/air secondary batteries-stability of the nasicon-type lithium ion conducting solid electrolyte in alkaline aqueous solutions, J. Power Sources **196** (2011) 5128–5132.

[57] E. Dashjav, Q.L. Ma, Q. Xu, C.L. Tsai, M. Giarola, G. Mariotto, F. Tietz, The influence of water on the electrical conductivity of aluminum-substituted lithium titanium phosphates, Solid State Ionics 321 (2018) 83–90.

[58] Y. Benabed, et al., Assessing the Electrochemical Stability Window of NASICON-type Solid Electrolytes" Frontiers in Energy Research, vol. 9, 2021, 682008.

[59] G. Tan, F. Wu, L. Li, Y. Liu, R. Chen, Magnetron sputtering preparation of nitrogen-incorporated lithium–aluminum–titanium phosphate based thin film electrolytes for all-solid-state lithium ion batteries, J. Phys. Chem. C 116 (5) (2012) 3817–3826.

[60] B.J. Neudecker, N.J. Dudney, J.B. Bates, Lithium-free" thin-film battery with in situ plated Li anode, J. Electrochem. Soc. 147 (2) (2000) 517–523.

[61] J. Qin, et al., Anode-free rechargeable lithium metal batteries" adv, Met. Funct. Mater. **26** (2016) 7094–7102.

[62] K.L. Lee, J.Y. Jung, S.W. Lee, H.S. Moon, J.W. Park, Electrochemical characteristics and cycle performance of $LiMn_2O_4$/a-Si microbattery, J. Power Sources 130 (1–2) (2004) 241–246.

[63] H. Otsuji, K. Kawahara, T. Ikegami, K. Ebihara, $LiMn_2O_4$ thin films prepared by pulsed laser deposition for rechargeable batteries, Thin Solid Films 506 (2006) 120–122.

[64] P. Liu, J.G. Zhang, J.A. Turner, C.E. Tracy, D.K. Benson, Lithium-manganese-oxide thin-film cathodes prepared by plasma-enhanced chemical vapor deposition, J. Electrochem. Soc. 146 (6) (1999) 2001–2005.

[65] J.B. Bates, N.J. Dudney, B.J. Neudecker, F.X. Hart, H.P. Jun, S.A. Hackney, J. Electrochem. Soc. 147 (2000) 59.

[66] A. Alexander, Delluva, jessica dudoff, glenn teeter, and adam holewinski. Cathode interface compatibility of amorphous $LiMn_2O_4$ (LMO) and $Li_7La_3Zr_2O_{12}$ (LLZO) characterized with thin-film solid-state electrochemical cells, ACS Appl. Mater. Interfaces 12 (2020) 24992–24999.

[67] N.J. Dudney, Solid-state thin-film rechargeable batteries, Mater. Sci. Eng. B-Solid State Mater. Adv. Technol. 116 (3) (2005) 245–249.

[68] Y. Ren, T. Liu, Y. Shen, Y. Lin, C.W. Nan, Chemical compatibility between garnet-like solid state electrolyte $Li_{6.75}La_3Zr_{1.75}Ta_{0.25}O_{12}$ and major commercial lithium battery cathode materials, J. Materiomics **2** (2016) 256–264.

[69] T. Mousavi, X. Chen, C. Doerrer, B. Jagger, S.C. Speller, C.R.M. Grovenor, Fabrication of $Li1_{+x}Al_xGe_{2-x}(PO_4)_3$ thin films by sputtering for solid, Solid State Ionics 354 (2020), 115397.

[70] D. Goonetilleke, N. Sharma, J. Kimpton, J. Galipaud, B. Pecquenard, F. Le Cras, Insight into the formation of lithium alloys in all-solid-state thin film lithium batteries, Front. Energy Res. 6 (2018) 64.

[71] Y.C. Lam, H.Y. Zheng, R.T. Tjeung, X. Chen, Seeing the invisible laser markings, J. Phys. D Appl. Phys. 42 (2009), 042004.

[72] W. Yan, H. Li, J. Liu, J. Guo, EPMA and XRD study on nickel metal thin film for temperature sensor, Sensor. Actuator. 136 (2007) 212–215.

[73] L. Tian, A. Yuan, Electrochemical performance of nanostructured spinel LiMn2O4 in different aqueous electrolytes, J. Power Sources 192 (2009) 693–697.

[74] X. Liu, J. Tan, J. Fu, R. Yuan, H. Wen, C. Zhang, Facile synthesis of nanosized lithium-ion-conducting solid electrolyte $Li_{1.4}Al_{0.4}Ti_{1.6}(PO_4)_3$ and its mechanical nanocomposites with $LiMn_2O_4$ for enhanced cyclic performance in lithium ion batteries, ACS Appl. Mater. Interfaces **9** (2017) 11696–11703.

[75] Q. Yu, D. Han, Q. Lu, Y.-B. He, S. Li, Q. Liu, C. Han, F. Kang, B. Li, Constructing effective interfaces for $Li_{1.5}A_{l0.5}Ge_{1.5}(PO_4)_3$ pellets to achieve room-temperature hybrid solid-state lithium metal batteries, ACS Appl. Mater. Interfaces **11** (2019) 9911–9918.

[76] Z. Li, S. Zhang, K. Qian, T. Li, G. Wei, F. Kang, Efficient Construction of a C60 Interlayer for Mechanically Robust, Dendrite-free, and Ultrastable Solid-State Batteries vol. **23**, iScience, 2020, 101636.

[77] A Das, P.S.R. Krishna, M Goswami, M Krishna, Structural analysis of Al and Si substituted lithium germanium phosphate glass-ceramics using neutron and X-ray diffraction, Solid State Chem. 271 (2019) 74–80.

[78] P. Tarte, A. Rulmont, C. Merckaert-Ansay, Vibrational spectrum of nasicon-like, rhombohedral orthophosphates $MIMIV_2(PO_4)_3$, Spectrochim. Acta Mol. Spectros 42 (1986) 1009–1016, 1986.

[79] B.E. Francisco, C.R. Stoldt, J.C. M'Peko, Lithium-ion trapping from local structural distortions in sodium super ionic conductor (NASICON) electrolytes, Chem. Mater. 26 (2014) 4741–4749.

[80] S.V. Pershina, A.A. Pankratov, E.G. Vovkotrub, B.D. Antonov, Promising high-conductivity Li1.5Al0.5Ge1.5(PO4)3 solid electrolytes: the effect of crystallization temperature on the microstructure and transport properties, Ionics 25 (2019) 4713–4725.

[81] M. Kazemian Abyaneh, T. Araki, B. Kaulich, A sub-microanalysis approach in chemical characterisation of gold nanorods formed by a novel polymer-immobilised gold seeds base, Nanomaterials 7 (10) (2017) 331.

[82] M. Lerotic, n.d. https://2ndlookconsulting.com/, 2nd Lookd Consulting

[83] Nancy J. Dudney, Evolution of the lithium morphology from cycling of thin film solid state batteries, J. Electroceram. 38 (2017) 222–229.

[84] S.O. Kucheyev, T.F. Baumann, Y.M. Wang, Y. van Buuren, J.F. Poco, J. H. Satcher Jr., A. Hamza, Monolithic, high surface area, three-dimensional GeO_2 nanostructures, Appl. Phys. Lett. 88 (2006), 103117.

[85] L. Armelao, F. Heigl, P.-S.G. Kim, R.A. Rosenberg, T.Z. Regier, T.-K. Sham, Visible emission from GeO_2 nanowires: site-specific insights via X-ray excited optical luminescence, J. Phys. Chem. C 116 (2012) 14163–14169.

[86] D.-Y. Cho, I. Valov, J. van den Hurk, S. Tappertzhofen, R. Waser, Direct observation of charge transfer in solid electrolyte for electrochemical metallization memory, Adv. Mater. 24 (2012) 4552–4556.

[87] K.V. Mitrofanov, A.V. Kolobov, P. Fons, X. Wang, J. Tominaga, Y. Tamenori, T. Uruga, N. Ciocchini, D. Ielmini, Ge L3-edge x-ray absorption near-edge structure study of structural changes accompanying conductivity drift in the amorphous phase of $Ge_2Sb_2Te_5$, J. Appl. Phys. 115 (2014), 173501.

[88] J.A. McLeod, J. Zhao, L. Yang, Y. Liu, L. Liu, Structural evolution of reduced GeO_x nanoparticles, Phys. Chem. Chem. Phys. 19 (2017) 3182–3191.

[89] R. Qiao, Y.-D. Chuang, S. Yan, W. Yang, Soft X-ray irradiation effects of Li_2O_2, Li_2CO_3 and Li_2O revealed by absorption spectroscopy, PLoS One 7 (2012), e49182.

[90] J. Wolfenstine, J.L. Allen, J. Read, J. Sakamoto, Chemical stability of cubic $Li_7La_3Zr_2O_{12}$ with molten lithium at elevated temperature, J. Mater. Sci. (2013) 48, 5846–5851.

[91] Y. Zhu, J.G. Connell, S. Tepavcevic, P. Zapol, R. Garcia-Mendez, N.J. Taylor, J. Sakamoto, B.J. Ingram, L.A. Curtiss, J.W. Freeland, D.D. Fong, Ne.M. Markovic dopant-dependent stability of garnet solid electrolyte interfaces with lithium metal, Adv. Energy Mater. 9 (11) (2019), 1803440.

[92] X. Cao, Y. Cao, H. Peng, Y. Cao, H. Zhu, N. Wang, X. Dong, C. Wang, Y. Liu, J. Wu, Y. Xia, A new germanium-based anode material with high stability for lithium-ion batteries, ACS Sustainable Chem. Eng. 9 (2021) 11883–11890.